Regadío Carretero, A. [et al.]. 2020, "Trajectory determination of muons using scintillators and a novel self-organizative map", Nuclear Instruments and Methods in Physics Research Section A: Accelerators, Spectrometers, Detectors and Associated Equipment, vol. 973, art. no. 164166.

Available at https://doi.org/10.1016/j.nima.2020.164166

(Article begins on next page)

Trajectory determination of muons using scintillators and a novel self-organizative map

Alberto Regadío[a,*], J. Ignacio García Tejedor[c], Sindulfo Ayuso[b,d], Óscar García Población[c], Juan José Blanco[d], Sebastián Sánchez-Prieto[c], Óscar Rodriguez Polo[c]

[a]*Electronic Technology Area, Instituto Nacional de Técnica Aeroespacial, 28850 Torrejón de Ardoz, Spain*
[b]*Equipment and Systems Test Department, Instituto Nacional de Técnica Aeroespacial, 28850 Torrejón de Ardoz, Spain*
[c]*Department of Computer Engineering, Space Research Group, Universidad de Alcalá, 28805 Alcalá de Henares, Spain*
[d]*Department of Physics and Mathematics, Space Research Group, Universidad de Alcalá, 28805 Alcalá de Henares, Spain*

Abstract

In this work we propose a method for the determination of the impact point of muons in scintillators using a novel type of self-organizative maps called Self-Equalizing Map (SEM) and comparing the relative pulse height obtained by four photomultipliers (PMTs) at each scintillator. Using two 1 m^2 scintillators and calculating the impact point in both of them, we can also estimate the angle of incidence of these particles. This method has been specifically designed for a muon telescope called MITO (Muon Impact Tracer and Observer) which is part of the ORCA (Antarctic Cosmic Ray Observatory). Data from tests using MITO in Livingston Island, Antarctica have been used to evaluate the feasibility of this method. The obtained directions have been found to be consistent with the expected incident directions of atmospheric muons produced by the interaction between CRs and atmospheric atoms.

Keywords: Digital pulse processing, Instrumentation, Muon detector, Scintillator, Self-organizative map, Neural Network

1. Introduction

Primary Cosmic Ray (CRs) and Solar Energetic Particles (SEPs) interact with air nuclei when they arrive at the top of Earth's atmosphere, producing secondary CRs. These secondary CRs, in turn, can interact with other nuclei and produce additional secondary particles. CRs and SEPs with energies above 500 MeV can produce secondary particles that can be measured by instruments operating at ground level. The CR secondaries most commonly measured at ground level are pions, muons, neutrons, protons, electrons and gammas being the muons the most abundant ones.

*Corresponding Author
Email addresses: regadioca@inta.es (Alberto Regadío), ignacio.garcia@uah.es (J. Ignacio García Tejedor), sindulfo.ayuso@edu.uah.es / ayusogs@inta.es (Sindulfo Ayuso), oscar.gpoblacion@uah.es (Óscar García Población), juanjo.blancoa@uah.es (Juan José Blanco), sebastian.sanchez@uah.es (Sebastián Sánchez-Prieto), o.rodriguez@uah.es (Óscar Rodriguez Polo)

The main responsible of muon flux at ground level are primary CRs with energies from tens to hundreds of GeV. Otherwise, neutrons observed by neutron monitors at ground level are produced by primary CRs with energies from 500 MeV up to 50 GeV, that is around the detection limit of neutron monitors. Therefore, muon and neutron observations at ground level are complementary in this primary CR range of energies [1]. On the other hand, while the arrival direction of CRs at the magnetosphere limit is almost isotropic, there are studies that indicate that sometimes that isotropy breaks slightly in favor of certain directions as a result of the arrival of huge magnetic structures at Earth's orbit, such as magnetic clouds embedded in interplanetary coronal mass ejections [2, 3]. Both muon flux measurement and determination of arrival direction at Earth's surface is typically performed by telescope arrays, for instance, the Nagoya Multi-directional Muon Telescope [4], or the GRAPES-3 Experiment [5]. However, the Muon Impact Tracer and Observer (MITO) is a single telescope designed to measure both muon flux and incident directions. In this telescope, the incident trajectory is derived from the muon impact point observed at two piled 1 m^2 scintillators [6], allowing the study of predominant directions. MITO is part of ORCA (Antarctic Cosmic Ray Observatory), which has been recently deployed by the University of Alcal at the Juan Carlos I Scientific Spanish Base, in Antarctica [7].

ORCA is a combination of a neutron monitor, NEMO, which is a direct heritage of CaLMa (Castilla-La Mancha Neutron Monitor [8], and the aforementioned MITO muon telescope. Its main objectives are to measure the flux of CRs in a region not covered by the Neutron Monitor Data Base (NMDB) and to study solar activity, which can be inferred from CR flux temporal variations. In this article, though, we will focus on MITO.

Muon tracking has traditionally been performed using multiple scintillators laid out in a two layer matrix (for instance, two layers of 6×6 scintillators), separated by a lead layer to filter out lower energy particles, with a photomultiplier (PMT) gathering the light generated at each scintillator. Another muon trackers are Nagoya (6×6 array of 1m^2 detectors) [4], São Martinho da Serra (two layers of 4×8 m with scintillators of 1 m^2) and Kuwait telescope (3×5×1 m with an intermediate lead layer) among others. When a coincidence is registered between two detectors, one at each layer, a trajectory can be determined limited by the resolution provided by each scintillator matrix and the distance between them. Apart from the resolution limitation, these instruments are usually very large and their construction cost is also very high, so another approach is to use just two large scintillators instead of two scintillator matrices, and determine the impact point at each of them in order to calculate a trajectory [9]. This is also the approach used in MITO, which obtains the point of impact by comparing the level of the pulses detected in several PMTs.

Basically, MITO is composed by a stack of two devices 136.5 cm apart from each other, each of them consisting of a scintillator and four photomultiplier tubes gathering the light emanating from its lateral sides. This allows the determination of the particle impact point at each device by means of pulse height analysis; and when the point of impact on each device is found, the angle of incidence of the particle can be obtained [10]. MITO will be described in detail in Section 2.

However, the determination of the impact position at each plane as a function of the measured pulse heights is difficult, not only because of the difficulty of developing a reliable reconstruction algorithm, but also because the measurement depends on multiple factors such as the response linearity of each PMT and the associated electronics or the ambient temperature. Furthermore, the response depends on the specific plane and PMT. On the other hand, the instrument would require a precise calibration process that should be repeated over time to ensure correct results as operating conditions change. What is proposed in this manuscript is a method that facilitates the determination of the point of impact and avoids this need for calibration, taking into account that the expected distribution of impact points follows a certain criteria obtained by simulation. To do so, we use a novel self-organize map called Self-Equalizing Map (SEM) that modifies the distribution function obtained by a simple reconstruction algorithm to tailor it to the expected distribution. The use of neural networks on particle detectors is not new, as they have been used to discriminate neutrons and gamma rays in scintillators [11] and more recently to maximize the Signal-to-Noise Ratio (SNR) [12]. The method to find out the point of impact is described in Section 3.

Section 4 describes the results obtained in the determination of impact points and incidence angles obtained from data captured by MITO during several days at the scientific base Juan Carlos I, located in Livingston Island (Antarctica). Finally, Section 5 covers the conclusions.

2. The experiment

MITO is an instrument composed of two identical devices, each consisting of a organic scintillator and four PMTs tubes mounted in an aluminum chassis. Each Saint-Gobain BC-400 scintillator is made of polyvinyl toluene with 65% anthracene, and is shaped like a square prism of $100 \times 100 \times 5$ cm. The light yielded by the scintillator when a particle goes through it is transported via light guides and collected by 4 Hamamatsu R2154-02 PMTs, located in front of each lateral side of the prism, at each of the corners of the aluminum chassis as shown in Figure 1(a). The distance between opposite PMTs is therefore 200 cm. The acceptance angle is given by the dimensions and separations of each scintillator of the MITO instrument (Figure 1). The histogram of the simulated and real acceptance angles will be given in Section 4.

The two MITO devices are stacked with a separation of 136.5 cm as depicted in Figure 1(b), and there is a 10 cm lead layer belonging to the neutron monitor that is placed between them, which is part of NEMO as shown in Figure 2. More technical information about this instrument can be found in [10].

When a particle impacts a scintillator, light is produced and the PMTs gather the light emerging through the four lateral sides simultaneously, subsequently generating a pulse which is captured by the data acquisition module (ARACNE), which has been configured specifically for this instrument [10]. This module works by sampling all eight pulses from the PMTs in parallel using a multichannel high-speed and high-resolution

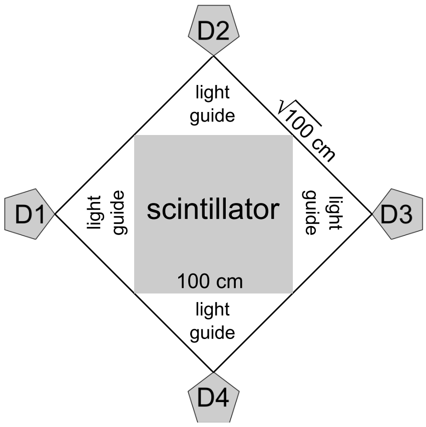

(a)

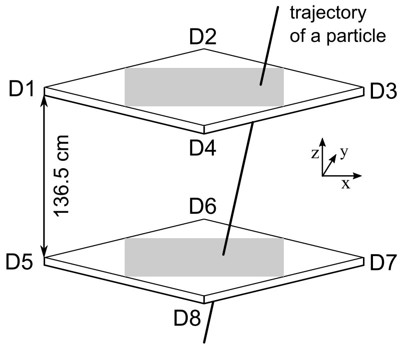

(b)

Figure 1: (a) Configuration of one of MITO's planes including the scintillator, the four PMTs (D1, D2, D3, D4) and light guides; (b) Layout of the stacked detectors to determine muon trajectory.

Figure 2: ORCA setup, including the two MITO devices at the top and bottom and NEMO in between.

Analog-to-Digital Converter (ADC) and doing all the pulse detection, discrimination, and pulse height analysis digitally. To achieve this, it uses specifically designed IPCores in a Field Programmable Gate Array (FPGA) and data acquisition and post-processing software running in an embedded Single Board Computer (SBC). A more detailed description of the ARACNE platform is foreseen in a future paper.

Consequently, the device monitors all channels simultaneously to detect a pulse on any channel, and when this happens the height of pulses on all channels is determined and stored. It is possible to store data only when the pulses happen in coincidence, lessening the probability of independent random background events or reducing the probability of a measurement being triggered by unrelated particles. The coincidence time window in the acquisition system used to gather the training data was 875 ns, and given that the experimental average event rate for the top and bottom scintillators at the time of the experiment have been measured at 2436 and 1906 counts per minute respectively, according to [1] the accidental rate is 8.12 counts per minute. Since the coincidence rate during the experiment has been measured at 320 counts per minute, this results in a 2.54% background event rate [13].

In order to obtain the pulse height and angle of incidence of the particles, these eight values per event have been processed as explained in the following section.

3. Procedure to measure the angle of incidence

The purpose of this section is to elaborate a method to calculate the angle of impact of muons based on their point of impact on each of the two MITO planes. To calculate this, we estimate the distance between the impact point and each of the four PMTs at each plane, which is a function of the pulse height of each captured event. MITO, in its configuration in Antarctica, has a 10 cm thick lead layer located above the bottom scintillator. Although certain muon dispersion is expected because of this lead layer, this dispersion is assumed to be negligible in the estimation of the angle of incidence.

Taking as reference Figure 1(a), in order to roughly estimate the point of impact, we assume, in a similar way to [14, 15], that the x-coordinate of this point (x_1) must increase as the height of the pulse captured by PMT D3 (I_3) is higher and the PMT opposite to it, in this case D1 (I_1), is lower; thus the difference between these signals gives an estimation of the x-coordinate, and to cancel out the average pulse amplitude, we divide the difference by $I_1 + I_3$, yielding a value between -1 and 1 that would correspond to the edges of the scintillator. This gives an approximation to x_1 equal to

$$x_1 = \frac{I_3 - I_1}{I_3 + I_1} \tag{1}$$

This formula is analogous on the y-axis (y_1) using PMTs D2 and D4

$$y_1 = \frac{I_2 - I_4}{I_2 + I_4} \tag{2}$$

and the coordinates in the other scintillator (x_2, y_2)

$$x_2 = \frac{I_7 - I_5}{I_7 + I_5} \tag{3}$$

$$y_2 = \frac{I_6 - I_8}{I_6 + I_8} \tag{4}$$

These simple formulae, which assume a linear relationship between distance and pulse height, do not calculate the impact coordinates; but to ensure that the impact point positions are ordered according to their distance to opposite PMTs. In other words, given two impacts and only considering the x-axis, the difference between their x_1 coordinates is not the real distance between both impacts in the x-axis, but yields the relative position between them. To precisely estimate impact coordinates based on the light collected, the use of more complex formulas would be necessary [16]. In our approach, to calculate the position of the impact points we will use these simple formulas and the self-organizing map explained the next section.

Applying these formulae on data collected along one day, (see Section 4 for a complete description of the setup experiment), we obtain the histograms of the impact points depicted in Figure 3, where asymmetries due to the different response from each PMT can be observed. The obtained histograms are very similar independently of the chosen day, since no important solar event happened that could affect the measurements in that period.

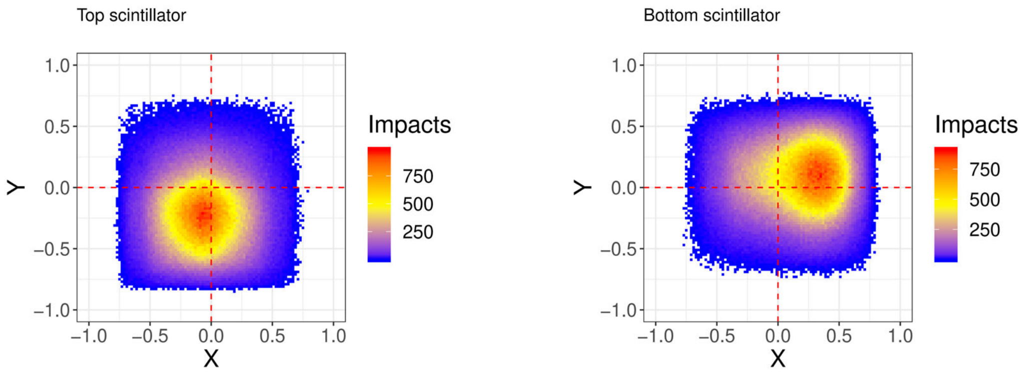

Figure 3: Histograms of the impact points obtained from the estimated positions calculated from the data collected in January 20, 2019, using equations (1-4). Note that X, Y do not indicate the absolute position of impact points but the relative position between them.

On the other hand, assuming muon impact points and incidence directions of the model presented in [17], that is, uniform distribution of ϕ and $\cos^2\theta$, a simulation yields the impact point histograms shown in Figure 4. These histograms have been obtained performing a simulation with "R" of 20,000,000 particle impacts taking into account the dimensions of the detector yields the distribution (Figure 1). It was performed by generating a random, evenly distributed impact point in the upper level between +0.5 m and −0.5 m from the center at a random 0-360 azimuthal angle ϕ, and also a random 0-90 zenith angle following a $\cos^2\theta$ distribution, and then calculating the impact point on the lower level following a straight trajectory.

These histograms show that the probability of impact in both planes is almost the same in all parts of the detector with a slight decay at the edges, due to the higher chance of particles crossing the top plane near the edge to fall off the bottom plane depending of their angle of incidence. In order to perform this simulation the dimensions given in Figures 1(a) and 1(b) were used.

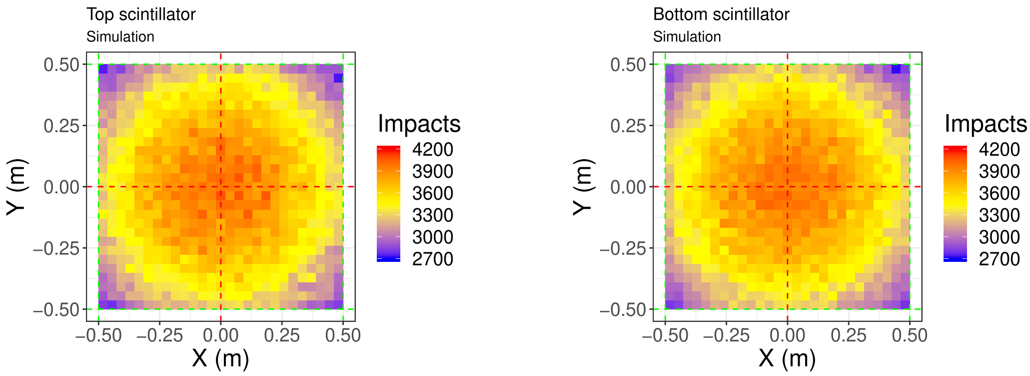

Figure 4: Impact points histograms obtained by means of simulation.

Clearly, histograms shown on Figure 3 and the distribution shown on Figure 4 do not match. To be able to calculate the coordinates x_1, y_1, x_2 and y_2 based on the eight values obtained from an event, the obtained distributions should be equal or at least very similar to simulations. With this goal in mind, we use a Self-Equalizing Map described below.

3.1. Self-Equalizing Map

A Self-Equalizing Map (SEM) is a novel type of artificial neural network that is trained using unsupervised learning to produce a concrete discretized distribution function (e.g. uniform) preserving the topological properties of the input space. In other words, it is a method to reorganize data without changing its order. Thus, for data to be applicable to a SEM, they must be well ordered, which means that if $x_1 < x_2$ is because it is so in reality although the distance between them is not $|x_1 - x_2|$. Sorting the impact points is the purpose of (equations 1, 2, 3 and 4).

In the same way as Self-Organizing Maps (SOMs), SEMs differ from other artificial neural networks in that they apply competitive learning instead back-propagation with gradient descent.

The purpose of using this network is to calibrate this detector without using radiation sources. For this, SEM is adjusted to achieve a well-known distribution obtained from simulations (Figure 4) that cover the entire scintillation area. For this, it must be trained with values captured by the uncalibrated PMTs (Figure 3) as explained in Section 3.1.1.

3.1.1. Learning rule

First, L is set to establish the number of neurons of the network (L^2), and the position of the neurons should be initialized covering the set of points used during the training process. The number of 4-side cells C thus will be $(L-1)^2$. Each cell is delimited by four coordinates given by the position of the neurons $\mathbf{p}_1$, $\mathbf{p}_2$, $\mathbf{p}_3$, $\mathbf{p}_4$ within which there will have to be a number of samples given by a discretized distribution. We also define the training rate α and the number of epochs.

In the network of Figure 5, $L = 5$. For this example we assume an uniform distribution, if the number of data samples is N, the number of samples per cell Λ must be

$$\Lambda^* = N/(L-1)^2 \tag{5}$$

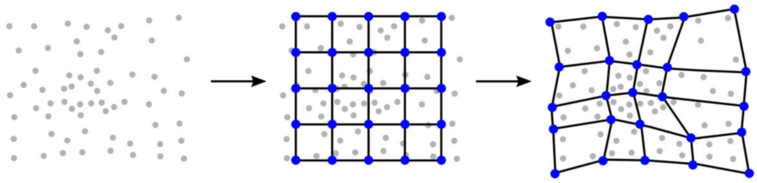

Figure 5: An illustration of a SEM training. The gray points are the distribution of the training data (left). At first (center), the SEM nodes are placed over the data space. After many iterations the grid tends to span the data distribution (right) where $\Lambda = \Lambda^* = 4$.

The number of samples per cell must be adjusted depending on the distribution, and could be defined as a constant or not, i.e $\Lambda^* = \Lambda^*(x, y)$ where $x, y \in 1, 2, \ldots, L$. For simplicity, we assume in this example that Λ^* is an uniform distribution, i.e. using (5).

The simulated distribution is used to calculate the expected number of impacts (Λ^*) on each cell of the non-deformed mesh; then, the actual data is applied to the mesh, which is subsequently deformed until the same number of impacts per cell is obtained in the deformed mesh. For this purpose, the number of samples Λ in each cell is counted after initialization. If the number is smaller than Λ^*, the cell is enlarged (Figure 6) proportionally to α, updating the neuron positions according to this formula:

$$\begin{aligned}
\mathbf{p}_1 &\leftarrow \mathbf{p}_1 + \alpha \cdot J \cdot \frac{1}{\sqrt{2}}(-1, 1) \\
\mathbf{p}_2 &\leftarrow \mathbf{p}_2 + \alpha \cdot J \cdot \frac{1}{\sqrt{2}}(1, 1) \\
\mathbf{p}_3 &\leftarrow \mathbf{p}_3 + \alpha \cdot J \cdot \frac{1}{\sqrt{2}}(-1, -1) \\
\mathbf{p}_4 &\leftarrow \mathbf{p}_4 + \alpha \cdot J \cdot \frac{1}{\sqrt{2}}(1, -1)
\end{aligned} \tag{6}$$

where J is the cost function defined as

$$J = \sum_{\text{each cell}} |\Lambda^* - \Lambda| \tag{7}$$

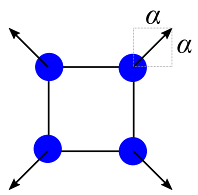

Figure 6: Enlargement of a cell to span the desired Λ^*.

We repeat this procedure for each cell of the matrix for a fixed number of iterations (epochs), which will result in the neurons moving around and reorganizing as shown in Figure 5. The equations used to sort the data do not affect the calculation of the impact point, as the SEM makes up for it; but in order to help the algorithm converge more quickly and since the expected impact distribution is known, the data used, represented in 3, is initially repositioned in the origin of the coordinate system in the center of the scintillator by subtracting the average pulse height from each PMT from the height of each pulse. It is important to note that this operation does not change the order in the data provided by the equations.

Once the process is over, a mesh is obtained which allows us to approximate the point of impact of a new event given the cell of this mesh where the impact falls, after calculating the position through the ordering equations described in Section 3 and the aforementioned correction.

It is important to note that, as long as the ordering equations used do their job and produce a well ordered distribution as described in Section 3, it doesn't matter which equations are used (although there are equations that make learning easier than others). They don't affect the precision of the calculated cell of impact position, since the SEM compensate it during training just like it compensates miscalibrations or differences in the system components.

The SEM training phase is based on a simulation that assumes the distribution for particles impacting the scintillator surface presented in [17] and real measurements that would produce such a distribution; a period of time with no solar events, or a period with a duration long enough to make the effect of noise and anisotropic events negligible. But once the training is done the SEM is static, and consequently it would map the measured data produced by an anisotropic event into an anisotropic trajectory distribution reflecting this fact.

A limitation of the SEM is the resolution to calculate impact positions and incidence angles, limited by the number of polygons. In addition, the mesh of the SEM is composed of polygons of four sides each. This is a handicap to separate the points according to a distribution, especially when there are high concentrations of points in certain regions. This causes the network to converge but has a constant error as will be seen in Figure 8. This constant error is decreased when L is reduced. However, it implies a reduced resolution of incidence angles as we will see in the next section. Another approach is substituting the straight lines of the mesh by curves; it can decrease this constant error but considerably increase the computation time and is not the object of study of this article. Finally, as previously explained, the data must be collected when there are no or spaced enough solar events as to be considered homogeneous (as in the simulations).

4. Results

Finally, a test with real data to check the proposed method has been performed. The data were collected using the MITO muon telescope from January 17, 2019 to January 20, 2019 in the Juan Carlos I scientific base, located in Livingston Island, Antarctica (S6239'46", W6023'20", 12 m asl).

As explained in Section 2, the raw data obtained from the eight PMTs was gathered using the ARACNE module and pulse height for each event in coincidence was stored in a text file that can be used repeatedly, ensuring that possible changes in the obtained results during the test are exclusively due to changes in the procedure explained in Section 3. The total number of sets of eight pulses captured in coincidence vary from 908,260 to 939,139 per day, and were captured during the full 24 hour period each day. The use of data extracted from whole days would compensate the possibility of anisotropies caused by Earth's rotation during training.

To perform the training process, a set of 200,000 pulses per scintillator, chosen randomly from the pulses of all days considered, were used. On one hand, if fewer pulses are used the map is less smooth since there is not enough pulses per square of the mesh. On the other hand, no more than 200,000 pulses were necessary because the SEM already converged and using more data did not improve the map. The training parameters were selected taking into account the convergence rate and the time taken for training; when α is low, the grid of the net becomes smoother but the number of epochs must be increased for the system to converge, so there is a trade-off between α and the number of epochs. For this experiment, $L = 28$ was chosen as it provided a good trade-off between impact resolution (729 cells of roughly 3.7×3.7 cm) and computation time, the number of epochs to train the SEM was set to 700, and the learning factor to $\alpha = 10^{-3}$. In all the tests carried out for this experiment the networks converged successfully. Using 200,000 pulses the training lasts 806 seconds using Matlab 2019 in a computer with an Intel Core i7 processor, which makes this method less accurate but a lot faster than manual calibration using a radiation source. Also, contrary to manual calibration, the detection process is not interrupted when the detector is calibrated using this method since, once calibrated, the pulses used for calibration can also be processed like the rest.

As explained in Section 1, since the goal of this method is determining the direction of the incident particles, two SEMs corresponding each one to a scintillator have been trained. The resulting grids are shown in Figure 7. As explained in Section 3.1, along the iterations the grid tends to homogeneously spread the data distribution and transform it in a distribution similar to the one of Figure 4, by means of a Λ^* impact distribution obtained from simulation.

In Figure 8, the evolution of the mean cost function $\overline{J}$ along the epochs is depicted. It shows that the network converges to a minimum of approximately 12% the initial $\overline{J}$ value. Additional tests with other data

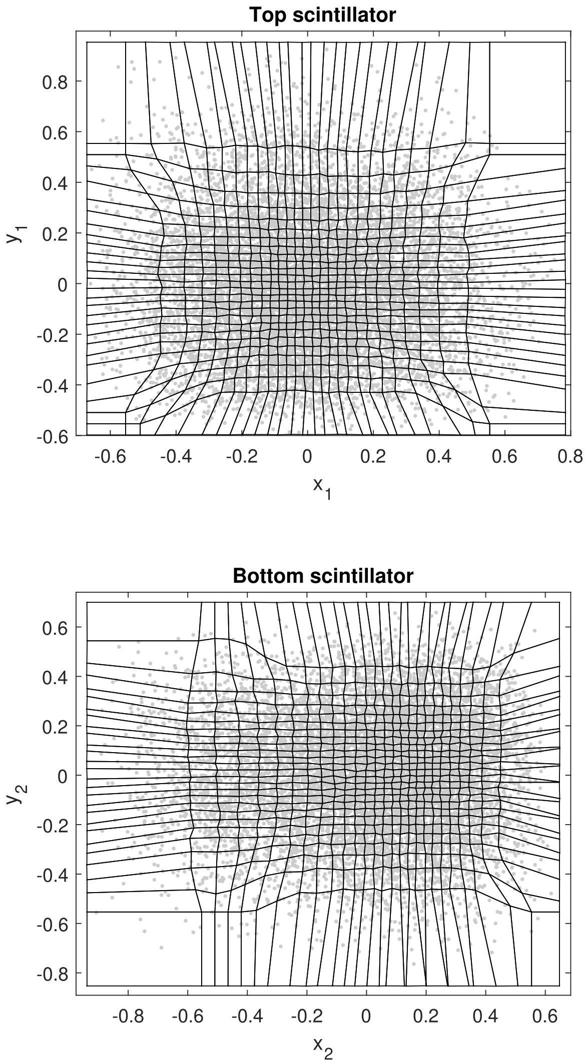

Figure 7: Grids created by the neurons after the training process. The gray points are the first 10000 samples. Note that x_1, y_1, x_2, y_2 do not indicate the absolute position of impact points but the relative position between them.

show similar decreasing exponentially in the cost function.

Once obtained, the SEMs can be used to directly determine the impact points at both scintillators given the pulse height values of a given event. Applying the test data to the SEMs, we can observe in Figure 9 that the impact point distribution is a lot more uniform that in Figure 3, and similar to Figure 4. It can be observed, though, that the decay of impact frequency at the edges is more pronounced than in Figure 4, a consequence of the algorithm struggling to adapt large empty areas of Figure 3 to the edges of the simulated

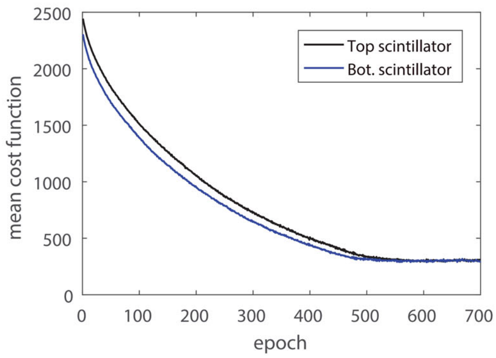

Figure 8: Learning rate for different values of both scintillators. The mean cost function is $\overline{J}$.

impact distribution.

As explained in Section 3, after obtaining the point of impact on each scintillator the angles of incidence in spherical coordinates (Figure 10) can be found.

Let us define $\Delta x = x_2 - x_1$ and $\Delta y = y_2 - y_1$. Once calculated, they are used together with the separation between planes ($\Delta z = 136.5$ cm) to obtain the incident direction in spherical coordinates ϕ and θ according to these formulas:

$$\begin{aligned} \phi &= \arctan \frac{\Delta y}{\Delta x} \\ \theta &= \arccos \frac{\Delta z}{\sqrt{\Delta x^2 + \Delta y^2 + \Delta z^2}} \end{aligned} \tag{8}$$

The histogram of ϕ and θ is shown in Figure 11(a), where the θ axis has been set so that each histogram cell represents the same solid angle. From this new perspective we can observe that higher values of θ are reached in diagonal directions (black dotted lines), which is logical because the length from corner to corner of each scintillator is $\sqrt{2}$ m, compared to 1 m from side to side. Thus, higher θ angles are possible (see Figure 1(a)).

The equivalent figure obtained from simulation is depicted in Figure 11(b). Note that the number of impacts in the color scale differ due to the different amount of impact points used in the simulation and the reconstruction. The simulation distribution is also more uniform; this is because it comes from the exact impact point coordinates obtained from simulation, while the Figure 11(a) distribution is obtained from a mesh adaptation in such a way that, when an impact is determined to have fallen into a specific cell, the center point of the cell is considered as the impact point. This quantization induced by the mesh implies that impact angles are also quantized, which produces the discontinuities. For example, when θ is near the vertical, there is very few possible ϕ angles and many trajectories are calculated as being in the 0-180 and 90-270 directions.

Since the zenith angle θ is the key to find anisotropies, another metric to evaluate the performance of SEM was the distribution of counts by θ in simulation and in real data. Results on simulations and real

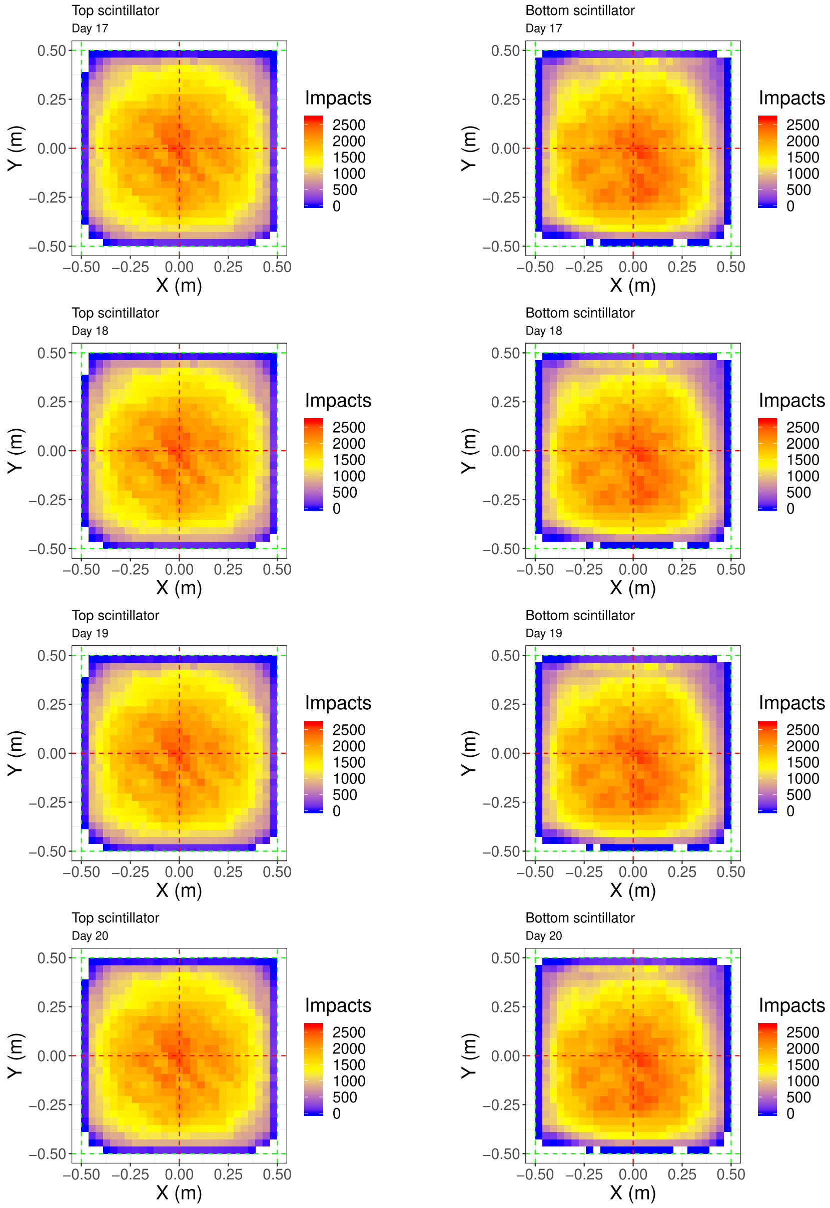

Figure 9: Final histograms. The histograms of scintillator 1 are located in the left column and the histograms of scintillator 2 are located in the right one.

pulses from four consecutive days were presented in Figure 12. These plots are not directly comparable to those presented in Figures 11(a) and 11(b), because they represent the number of impacts directly against the zenith angle of the trajectory without considering the dependence with the solid angle (see Figure 12). Nevertheless, it allows a direct comparison between the simulation and results obtained by using real data, showing the agreement between them.

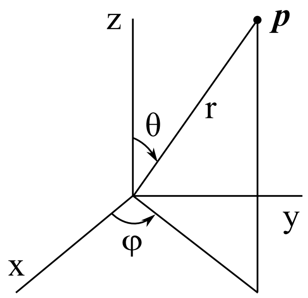

Figure 10: Spherical coordinates.

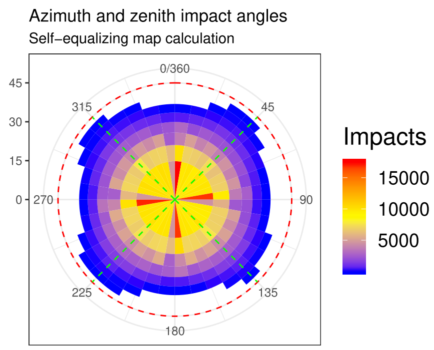

(a)

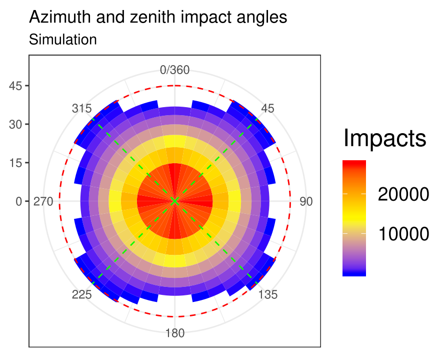

(b)

Figure 11: (a) Polar histograms of ϕ and θ of the experiment data. The number of impacts registered that day were 936,029; (b) Polar histograms of ϕ and θ of the simulated data of Figure 4 using 2,565,254 impacts.

5. Conclusions

We have developed a method based on a novel self-organizative map called Self-Equalizing Map (SEM) to calculate the point of impact of a particle in a scintillator. This map is trained using unsupervised learning to produce a specific discretized distribution function preserving the topological properties of the

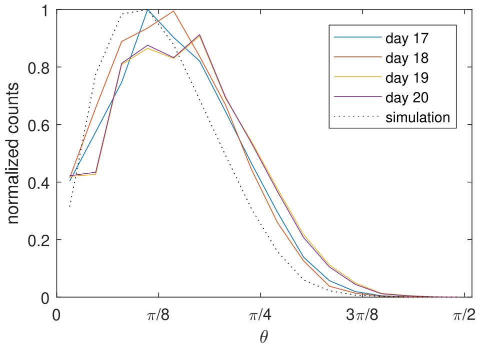

Figure 12: Histogram of θ vs. normalized counts for the four days (solid lines) and for the simulation of Figure 4 (dotted line).

input space. The learning process has been attained through the training of SEMs according to a previously generated simulation, assuming that the angle of incidence of muons is isotropic along one day. This method has been applied to data obtained from the MITO instrument, which consists of two stacked scintillators, in a real environment, to estimate the source direction of the incident muons detected. The obtained directions have been found to be consistent with the expected distributions. This method also has the advantage that it can be used remotely, so that if the instrument properties change along the time (e.g. changes of PMTs with temperature) it can be remotely recalibrated; which is useful if it is located in regions difficult to reach, such as Antarctica in this case.

Acknowledgements

Thanks to project CTM2016-77325-C2-1-P funded by Ministerio de Economía y Competitividad and by the European Regional Development Fund, FEDER.

References

[1] M. L. Duldig, Muon observations, 2000.

[2] F. Jansen, K. Munakata, M. Duldig, R. Hippler, in: ESA Space Weather Workshop: Looking towards a European Space Weather Programme.

[3] T. Kuwabara, J. W. Bieber, J. Clem, P. Evenson, R. Pyle, Space Weather 4 (2006) n/a–n/a.

[4] Nagoya experiment, http://www.stelab.nagoya-u.ac.jp/ste-www1/div3/muon/muon1.html, 2019.

[5] Grapes-3, https://grapes-3.tifr.res.in/, 2019.

[6] S. Ayuso, J. José Blanco, J. Medina, R. Gómez-Herrero, O. García-Población, I. García Tejedor, Geoscientific Instrumentation, Methods and Data Systems (2016).

[7] J. J. Blanco, O. García Población, J. I. García Tejedor, J. Medina, M. Prieto, A. López-Comazzi, S. Ayuso, R. Gómez-Herrero, C. Steigies, in: 36th International Cosmic Ray Conference (ICRC2019), volume 36 of *International Cosmic Ray Conference*, p. 1060.

[8] J. Medina, J. J. Blanco, O. García, R. Gómez-Herrero, E. J. Catalán, I. García, M. A. Hidalgo, D. Meziat, M. Prieto, J. Rodríguez-Pacheco, S. Sánchez, Nuclear Instruments and Methods in Physics Research, Section A: Accelerators, Spectrometers, Detectors and Associated Equipment (2013).

[9] D. Mahon, A. Clarkson, D. Hamilton, M. Hoek, D. Ireland, J. Johnstone, R. Kaiser, T. Keri, S. Lumsden, B. McKinnon, et al., Nuclear Instruments and Methods in Physics Research Section A: Accelerators, Spectrometers, Detectors and Associated Equipment 732 (2013) 408–411.

[10] S. Ayuso, J. I. García Tejedor, J. J. Blanco, R. Gómez Herrero, O. García Población, J. Medina, M. Prieto, A. López Comazzi, in: 36th International Cosmic Ray Conference (ICRC2019), volume 36 of *International Cosmic Ray Conference*, p. 180.

[11] G. Liu, M. D. Aspinall, X. Ma, M. J. Joyce, Nuclear Instruments and Methods in Physics Research, Section A: Accelerators, Spectrometers, Detectors and Associated Equipment (2009).

[12] A. Regadío, S. Sánchez-Prieto, L. Esteban, Nuclear Instruments and Methods in Physics Research, Section A: Accelerators, Spectrometers, Detectors and Associated Equipment (2019).

[13] M. Duldig, R. Jacklyn, in: International Cosmic Ray Conference, volume 4, p. 380.

[14] N. Hasebe, Y. Ezawa, H. Yoshii, T. Yanagimachi, Japanese Journal of Applied Physics (1988).

[15] A. Banu, Y. Li, M. McCleskey, M. Bullough, S. Walsh, C. Gagliardi, L. Trache, R. Tribble, C. Wilburn, Nuclear Instruments and Methods in Physics Research Section A: Accelerators, Spectrometers, Detectors and Associated Equipment 593 (2008) 399–406.

[16] Glenn G. Knoll, Radiation Detection and Measurement (4th Edition), 2010.

[17] J. Sullivan, Nuclear Instruments and methods 95 (1971) 5–11.